Electronic Supplementary Information (ESI) for Lab on a Chip

Electronic Supplementary Information

Spiral microchannel with ordered micro-obstacles for continuous and high-efficient particle separation

Shaofei Shen,[ab] Chang Tian,[c] Tianbao Li,[a] Juan Xu,[a] Shu-Wei Chen,[a] Qin Tu,[a] Mao-Sen Yuan,[a] Wenming Liu*[a] and Jinyi Wang*[ac]

[a]*College of Chemistry and Pharmacy, Northwest A&F University, Yangling, Shaanxi 712100, China. E-mail: liuwenming0229@nwsuaf.edu.cn, jywang@nwsuaf.edu.cn*

[b]*College of Life Sciences, Shanxi Agricultural University, Taigu, Shanxi 030801, China.*

[c]*College of Veterinary Medicine, Northwest A&F University, Yangling, Shaanxi 712100, China.*

Abstract. This supplementary information provides all the additional information as mentioned in the text.

Device fabrication

The microfluidic devices utilized for this study were fabricated using standard soft lithography with PDMS purchased from Momentive Performance Materials (Waterford, NY, USA). First, patterns for the microchannels were designed using AutoCAD software. Second, microchannels were printed on transparent films (MicroCAD Photomask, Ltd., Suzhou, China) to form a photomask. As a result, the mold was fabricated through a single step under UV light using SU8 photoresist (Microchem, MA, USA) on a BG401A mask aligner (7 mW cm^{-2}, CETC, China). Before fabricating the microfluidic device, the mold was exposed to trimethylchlorosilane vapor for 3 min. A well-mixed PDMS pre-polymer [RTV 615 A and B (10:1, w/w)] was poured onto the mold placed in a Petri dish to yield 3 mm-thick PDMS replica. After degassing, the mold was baked at 80 °C for 50 min. The PDMS replica was then peeled off the mold. Holes for inlets and outlets were punched with a metal pin. Afterward, the PDMS replica was trimmed, cleaned, and placed on a clean glass slide coated (3000 rpm, 60 s, ramp 15 s) with a PDMS pre-polymer [RTV 615 A and B (20:1, w/w)] that had been cured for 20 min in an oven at 80 °C. Finally, the microfluidic device was ready for use after baking at 80 °C for 48 h.

Numerical simulations

To evaluate fluid motion, vortex distribution in the microfluidic system, computational fluid dynamics (CFD) simulation was performed using ESI-CFD software (V2010.0, ESI CFD, Inc., Huntsville, AL). The simulation environment was verified for steady-state incompressible flows in the section of “Dean-like secondary flow flow acceleration”. Different flow rates were specified at the input, and the outlet was set to a fixed-pressure boundary condition. No slip boundary condition was applied at the channel walls. FLOW, TURBULENCE, and CHEM modules in CFD-ACE+ were used to explore fluid phenomena in the microchannels. Multiblock structured meshes with around 0.5 million cells were used, with near-wall refinement. Based on the finite volume method, the conservation of Navier–Stokes momentum in the device is described by

Equation (1) as follows:

$$\frac{\partial}{\partial t}(\rho\bar{V}) + \nabla \cdot (\rho\bar{V}V) = -\nabla P + \nabla \cdot \bar{\bar{\tau}} \quad (1)$$

The conservation of mass is described by the continuity Equation (2) as follows:

$$\frac{\partial \rho}{\partial t} + \nabla \cdot (\rho\bar{V}) = 0 \quad (2)$$

The local turbulent Reynolds number (Re_t) is expressed as follows:

$$Re_t = \frac{k^2}{v\varepsilon} \quad (3)$$

where ρ is fluid density; $\bar{V}$ is velocity vector; P is pressure; $\bar{\bar{\tau}}$ is stress tensor; k is turbulent kinetic energy; ε is rate of dissipation, t is time, ∇ is the standard spatial grad operator, and v is turbulent viscosity. The physical properties of water were applied to the fluids participating in the simulation (density p = 1000 kg m^{-3} and dynamic viscosity μ = 10^{-3} kg m^{-1} s^{-1}).

Focusing and isolation efficiency

The focusing efficiency of particles and rare cells were calculated using the following equations:

$$Focusing\ efficiency = \frac{n_{single\ -\ stream}}{n_{total}} \times 100\% \quad (4)$$

where $n_{single\text{-}stream}$ is the image numbers of single-stream focusing, n_{total} is total image numbers under identical operational conditions ($5000 < n_{total} < 6000$). Time-lapse fluorescence images of particles and rare cells were respectively obtained every 2s and 4s. Thousands of images were selected because they can demonstrate the stability of focusing efficiency more accurately under long-duration operation.

The collection efficiency and purity of mixed particles with three different sizes were calculated using the following equations:

$$Collection\ efficiency = \frac{n_{outlet}}{n_{inlet}} \times 100\% \quad (5)$$

$$Purity = \frac{n_{outlet}}{N_{outlet}} \times 100\% \quad (6)$$

where n_{outlet} is the number density of target particles collected from the target outlet; n_{inlet} is the number density of target particles in the original sample; N_{outlet} is the number density of total particles collected from the target outlet.

The collection efficiency, enrichment efficiency and purity of rare cells were calculated using the following equations:

$$Collection\ efficiency = \frac{n_{outlet1}R_{outlet1}}{n_{inlet}R_{inlet}} \times 100\% \quad (7)$$

$$Enrichment = \frac{R_{outlet1}}{R_{inlet}} \quad (8)$$

where $n_{outlet1}$ is the number density of blood cells, collected from the outlet 1, n_{inlet} is that in the original sample, $R_{outlet1}$ is the ratio of cancer cells to blood cells in a sample collected from the outlet 1, R_{inlet} is that in the original sample.

The rejection efficiency and plasma recovery of blood cells were calculated using the following equations:

$$Rejection\ efficiency = \frac{n_{inlet} - n_{outlet2} - n_{outlet3}}{n_{inlet}} \times 100\% \quad (9)$$

$$Plasma\ recovery = \frac{V_{outlet2} + V_{outlet3}}{V_{inlet}} \times 100\% \quad (10)$$

where $n_{outlet2}$ and $n_{outlet3}$ are the density of blood cells collected from the outlet 2 and 3

respectively; n_{inlet} is the density of blood cells in the original sample; $V_{outlet2}$ and $V_{outlet3}$ are the volumes of blood collected from the outlet 2 and 3 respectively; V_{inlet} is the volume of the original blood sample.

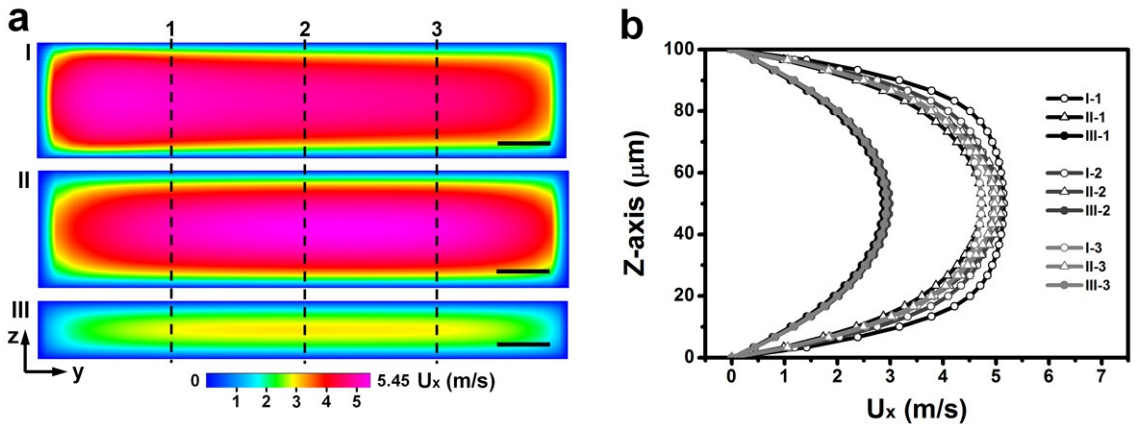

Fig. S1. Numerical simulation of fluid motion in x-axis in the channels. (a) Simulated fluid velocity field along the channels. i, ii, and iii represent fluid velocity field of channel cross-sections corresponding to the positions in Fig. 1a. The width of the wide and narrow regions in D-channel are 900 and 450 μm, respectively, the width of N-channel is either 450 or 900 μm, and the height of channels are totally 100 μm. The flow rate is 10 ml min^{-1}. The cross-sections were quartered for quantitative evaluation of local flow field. Scale bars, 45 μm in Fig. S1a-I and 1a-II, 90 μm in Fig. S1a-III. (b) Quantitative analysis of fluid velocity in x-axis of both D-channel and N-channel. The results correspond to the dotted lines in Fig. S1a.

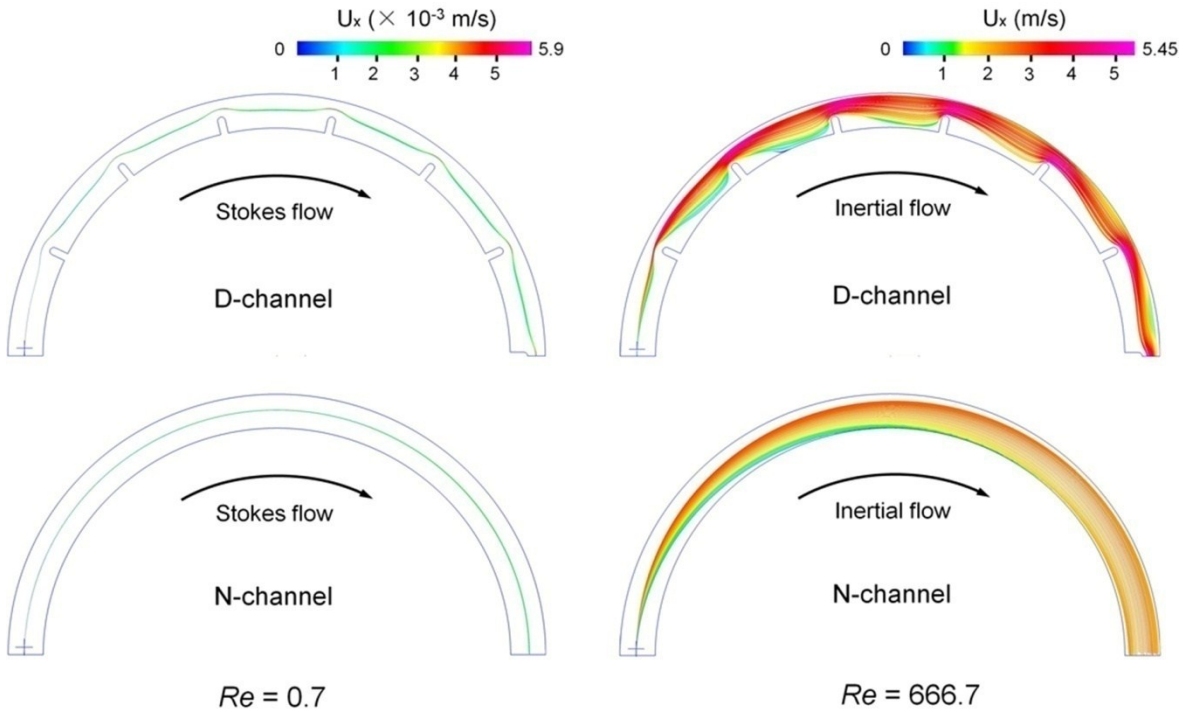

Fig. S2. Streamline distribution in D-channel and N-channel at a low flow rate of 10 μl min^{-1} (Re=0.7) and a high flow rate of 10 ml min^{-1} (*Re*=666.7) using computational simulation method of streamline trajectories (starting at the same position of inlet). There is almost no velocity change and lateral migration of streamlines after passing D-channel and N-channel under Stokes flow.

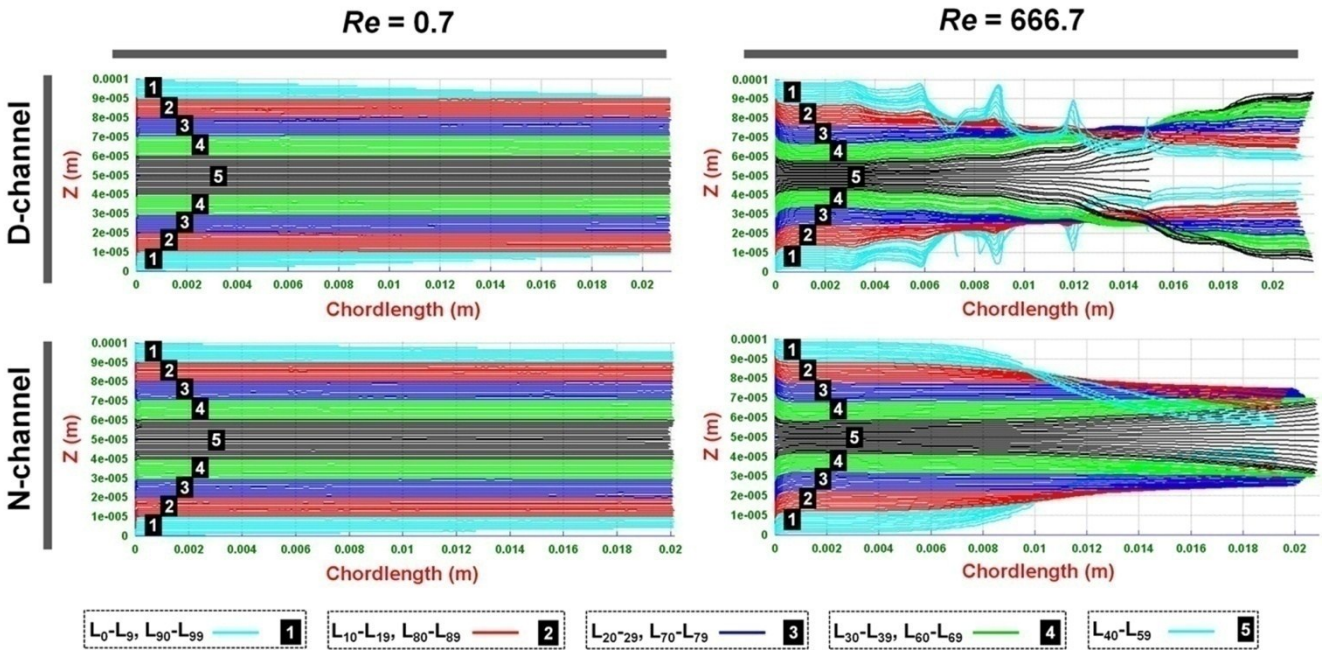

Fig. S3. Height distribution of a set of streamlines (starting at the same position of inlet corresponding to Fig. S2) in D-channel and N-channel under Stokes flow and inertial flow, respectively.

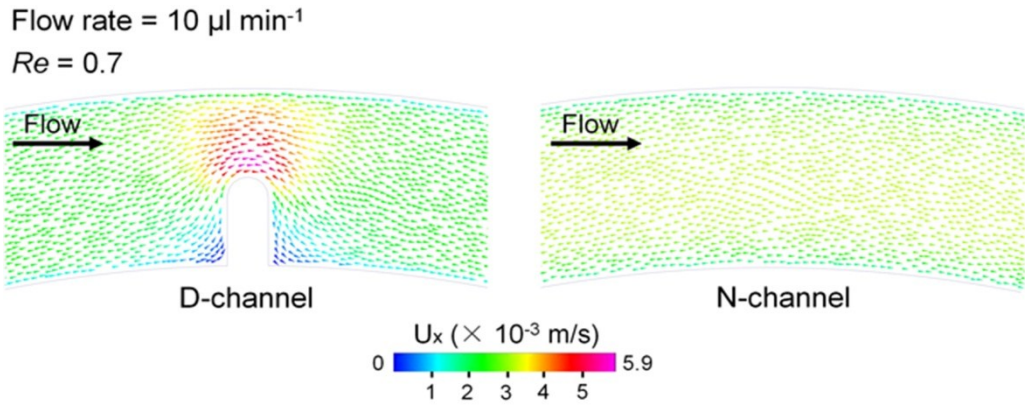

Fig. S4. Numerical simulation of velocity distribution in x-axis in D-channel and N-channel at a flow rate of 10 μl min^{-1} (Re=0.7).

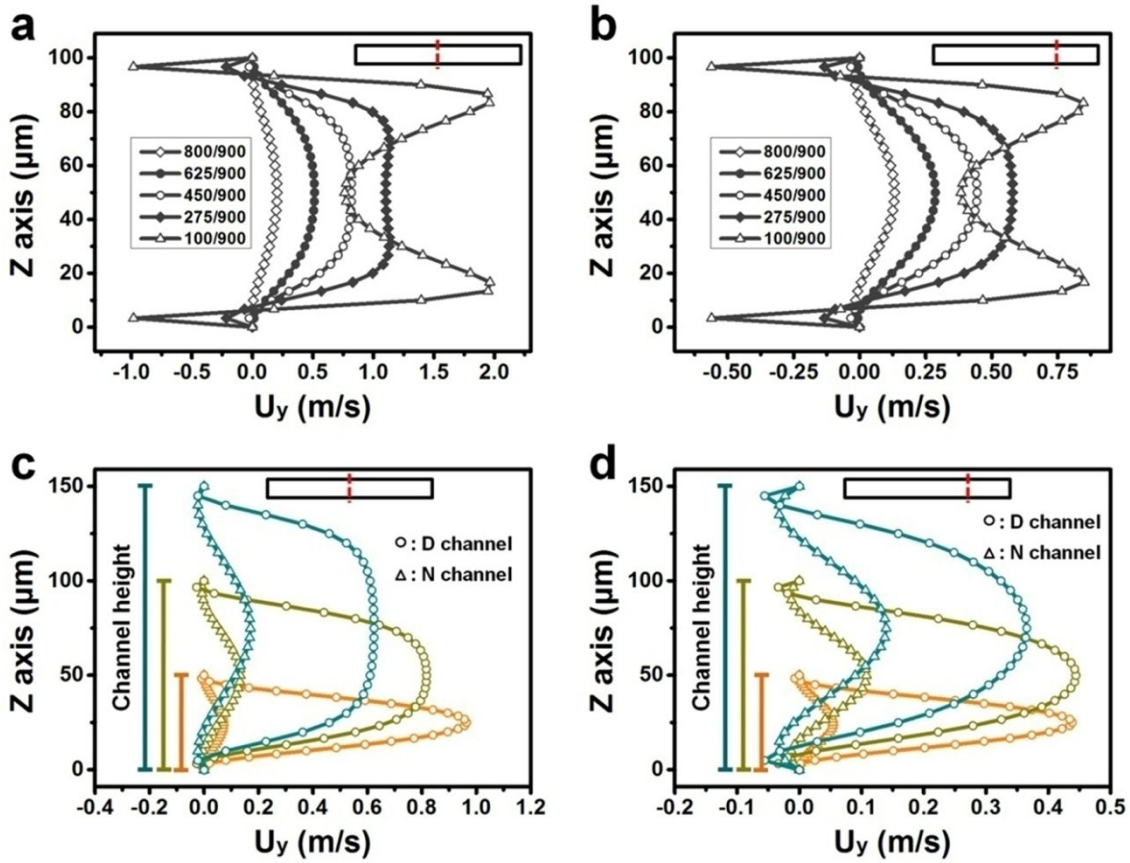

Fig. S5. Quantitative simulation of fluid motion under inertial flow condition. (a, b) Quantitative analysis of fluid velocity in y-axis at different positions in the narrow region of D-channel with different narrowing ratios from 1/9 to 8/9. (c, d) Fluid velocity in y-axis at different positions in the narrow region of D-channel with different heights (50, 100, and 150 μm). In Fig. S5a and 5c, the results were acquired from the same position as that marked by the dotted lines (i-2) in Fig. 1b. In Fig. S5b and 5d, the results were acquired from the same position as that marked by the dotted lines (i-3) in Fig. 1b. N-channel was set as a control.

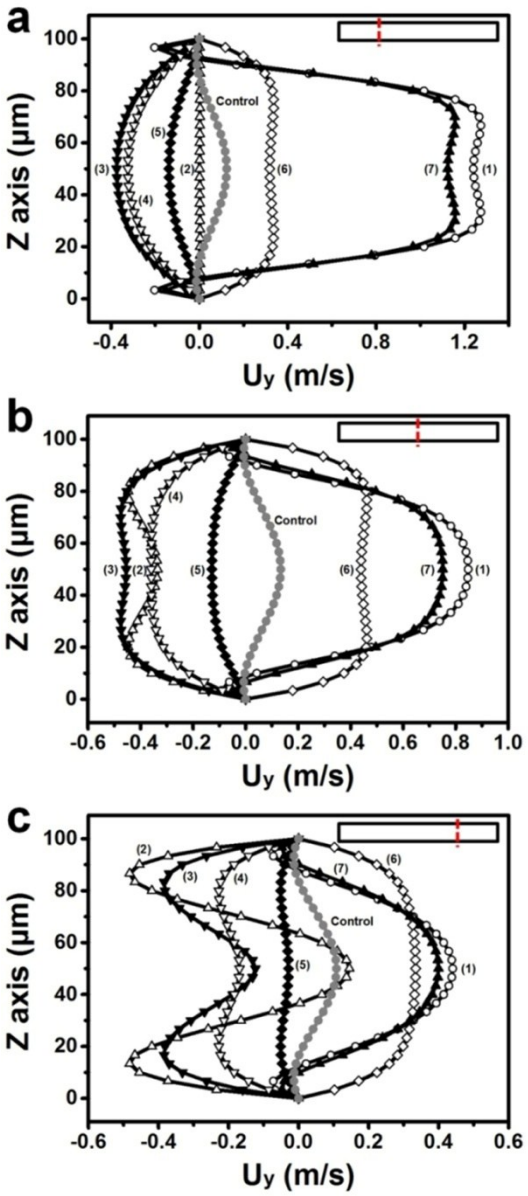

Fig. S6. Fluid velocity field of seven cross-sections in y-axis along D-channel (NR = 0.5). (a, b, c) In Fig. S6a, 6b and 6c, the results were acquired from the same position as that marked by the dotted lines (i-1, i-2, and i-3) in Fig. 1b, respectively. The numbers (1 to 7) were corresponding to the seven cross-sections along D-channel from upstream to downstream shown in Fig. 2e. N-channel was set as a control.

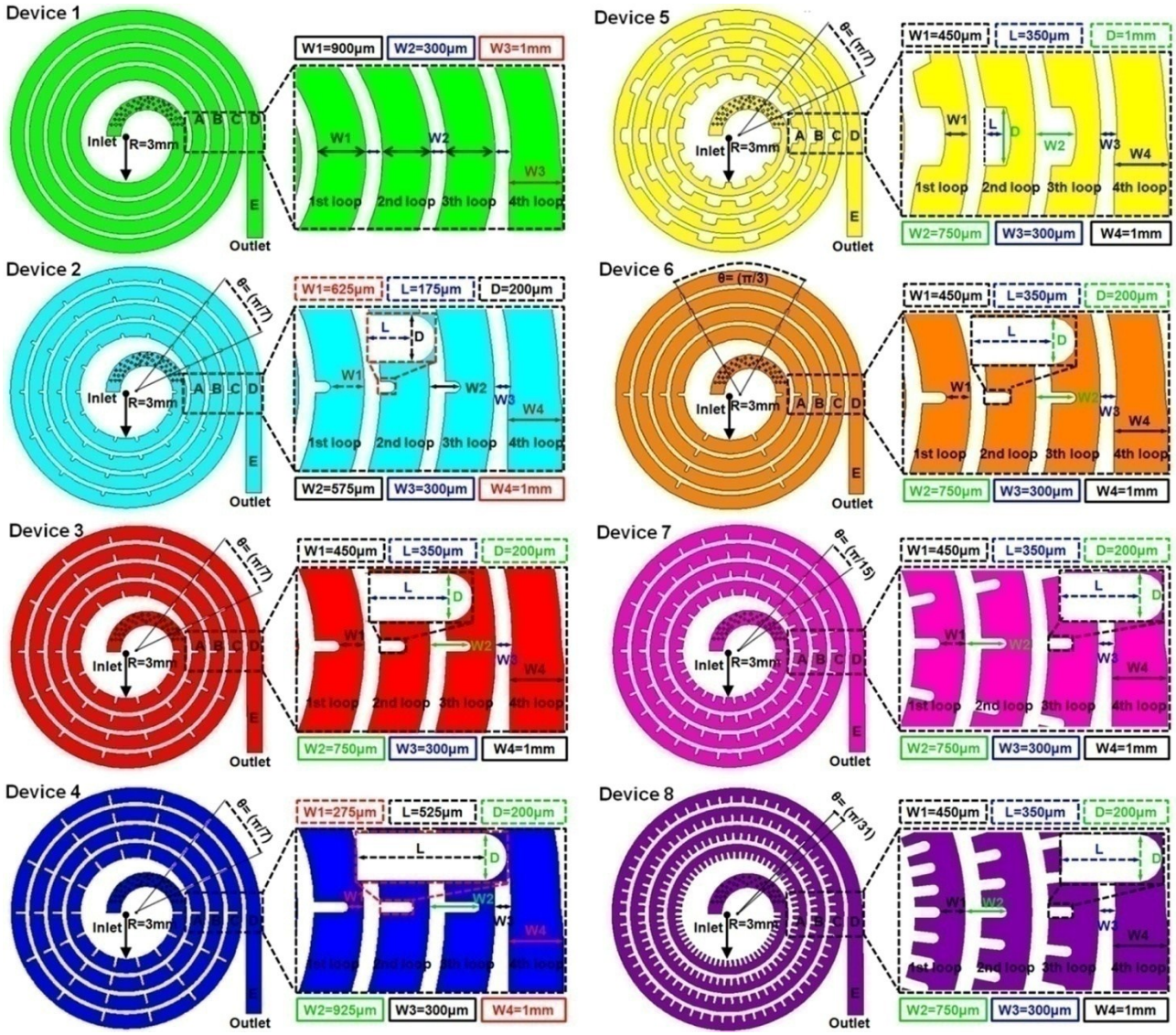

Fig. S7. Schematic diagram and design of eight microfluidic devices. Each of eight devices (device 1 to 8) consists of a low-aspect-ratio spiral microchannel with four loops, one inlet, and one outlet. The main microchannel structure is 900 μm in width, 100 μm in height, and with 3 mm initial radius of curvature. The distance between two adjacent loops is 300 μm. In outlet region, the microchannel gradually expands to 1 mm wide. Device 1, as a blank control, has not sequenced microbars in the microchannel (N-channel). The other 7 devices were designed with sequentially arranged microbars with different sizes in the microchannels. The amplifying images show detailed design parameters of different devices. The A, B, C, D, and E represent the observed regions of different loops (region A for the 1st loop, region B for the 2nd loop, region C for the 3th loop, region D for the 4th loop, and region E for the outlet region of the 4th loop) in the devices.

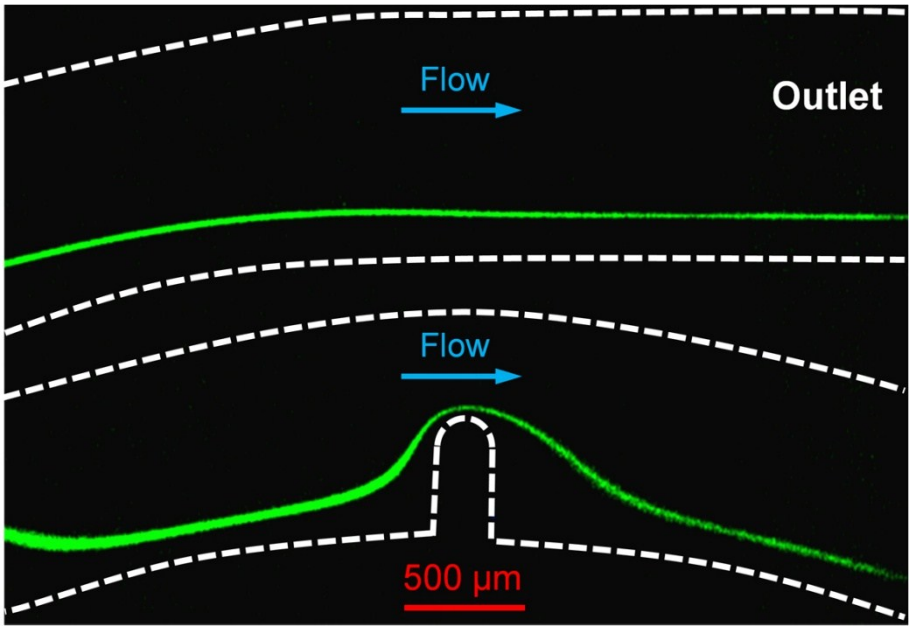

Fig. S8. Trajectories of fluorescent particles (15.5 μm in diameter) in the region C and D of device 3 under a flow rate of 2 ml min^{-1} (Re = 133.3).

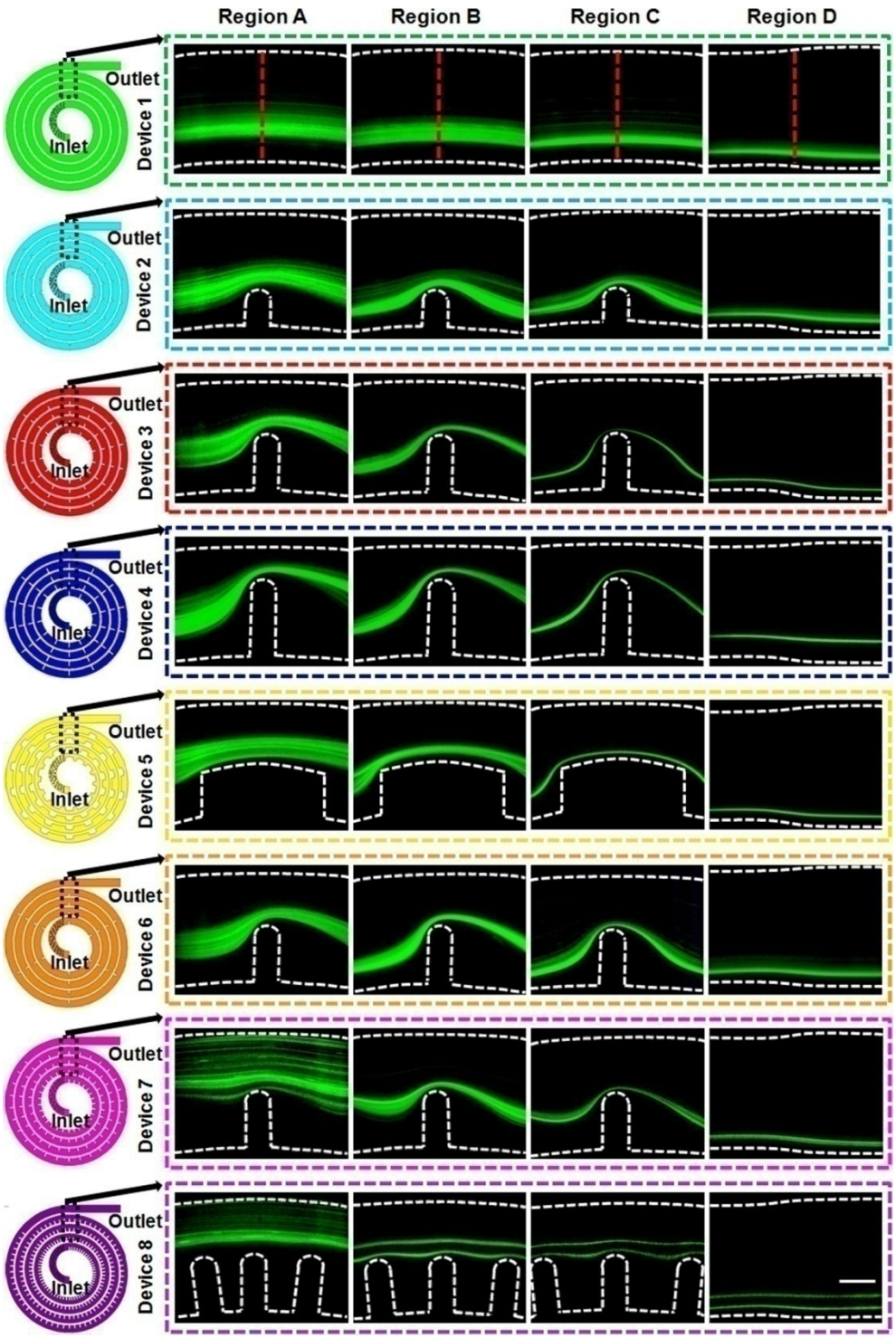

Fig. S9. Trajectories of fluorescent particles (15.5 μm in diameter) in the different regions of different devices under the same inertial flow condition (Re = 133.3, flow rate: 2 ml min^{-1}). Regions A, B, C and D correspond to the channel positions in Fig. S7. Red dotted lines are used to analyze fluorescent particle distributions at the same longitudinal positions. The analytical results are listed in Fig. S10. Scale bar, 300 μm.

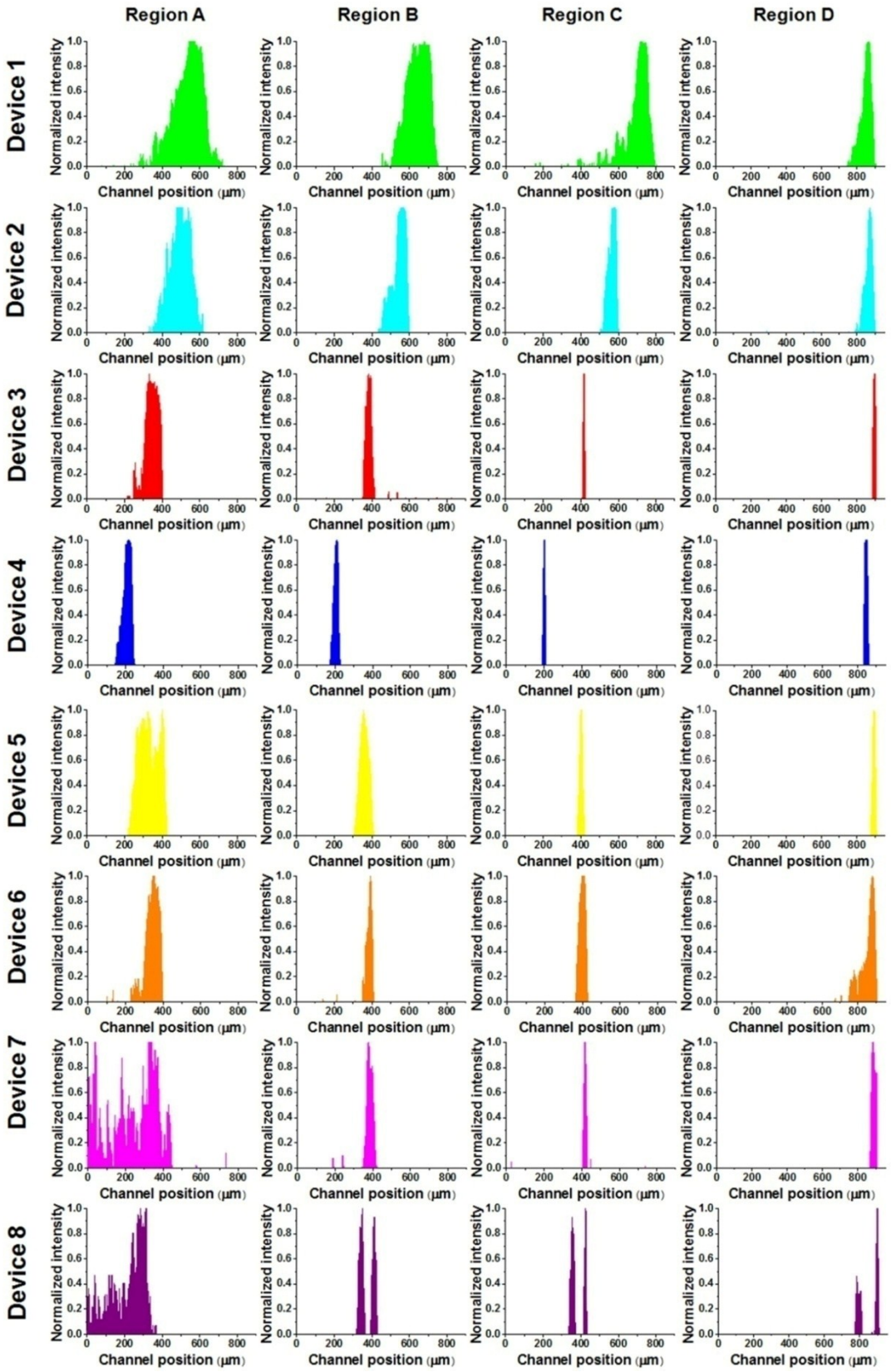

Fig. S10. Fluorescence intensity analysis of the fluorescent particle (15.5 μm in diameter) trajectories in the different regions of different devices under the same inertial flow condition (Re = 133.3, flow rate: 2 ml min^{-1}). The results correspond to the red dotted lines in Fig. S9.

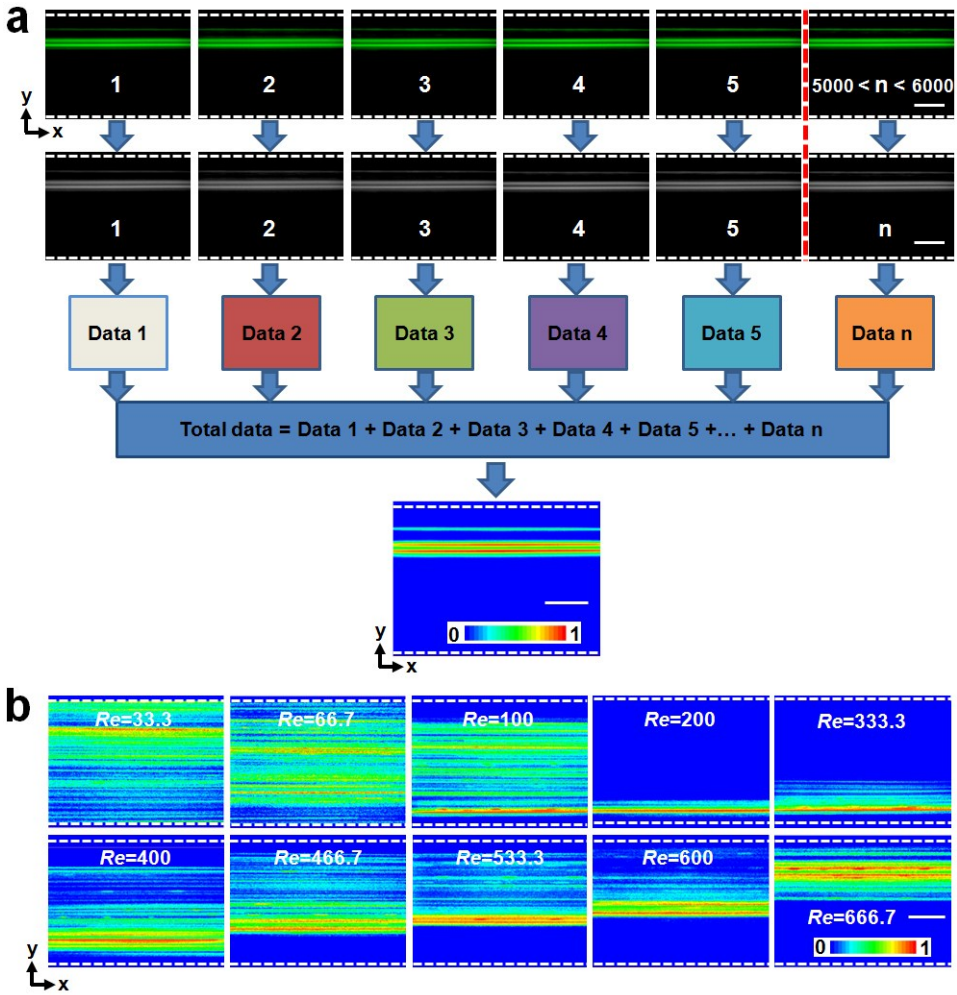

Fig. S11. Contour diagram-based particle focusing evaluation. (a) Principle of contour diagram formation for the fluorescent particle trajectories in the outlet region of device at a certain flow condition. For assessing the repeatability and stability of particle focusing operation, contour diagram was chosen because that it is able to present a combined particle trajectory from lots of images for one focusing experiment. Qualitative fluorescent particle trajectory can be depicted by contour diagram. In the beginning, a set of fluorescence images (5000–6000) repeatedly captured at the same position from the same particle focusing test. The fluorescence images were then converted to grayscale images and each pixel's data from images was extracted by using software Image-Pro® Plus 6.0. Finally, the calculated total data from thousands of fluorescence images for the single test of particle focusing was normalized and converted to a single image (contour diagram) by using software Origin 9. (b) Contour diagrams of the fluorescent particle trajectories in the outlet region of device 1 (as blank control) under different Re. White dotted lines indicate the positions of the channel walls. Scale bars, 300 μm.

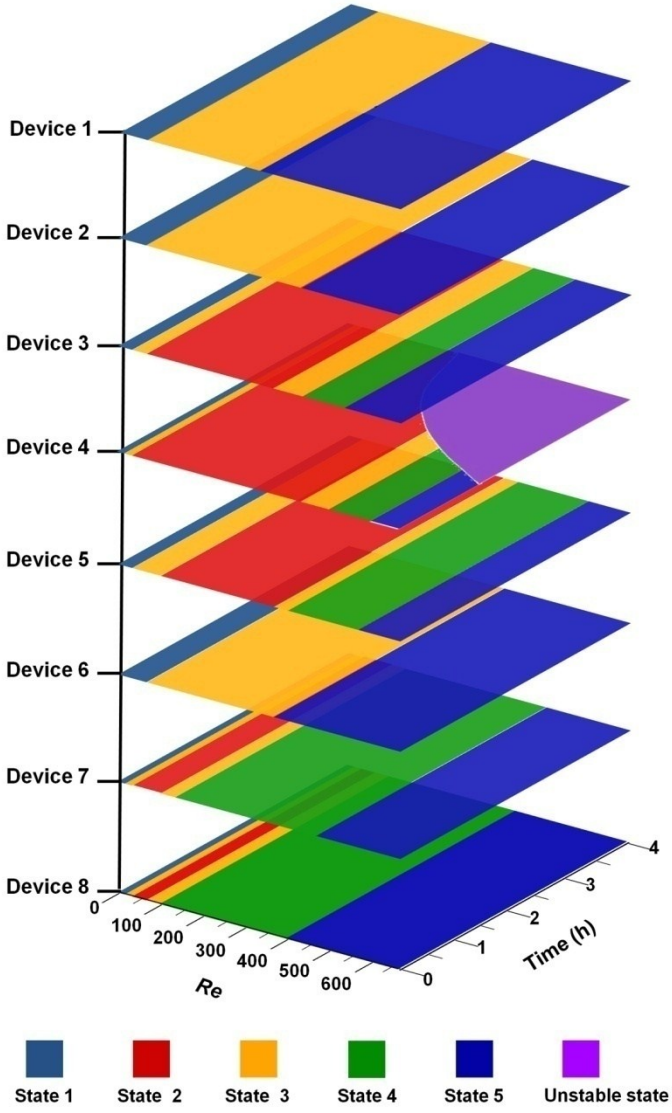

Fig. S12. Phase diagram for 15.5-μm particle trajectories in the outlet region of different devices under various flow conditions (Re = 0 to 666.7 corresponding to flow rates from 0 to 10 ml min^{-1}) and loading time (0 to 4 h). There were 6 states for particle trajectories (state 1: no focusing; state 2: single-stream focusing; state 3: single-stream focusing with particle dispersion; state 4: double-stream focusing; state 5: double-stream focusing with particle dispersion; and unstable state).

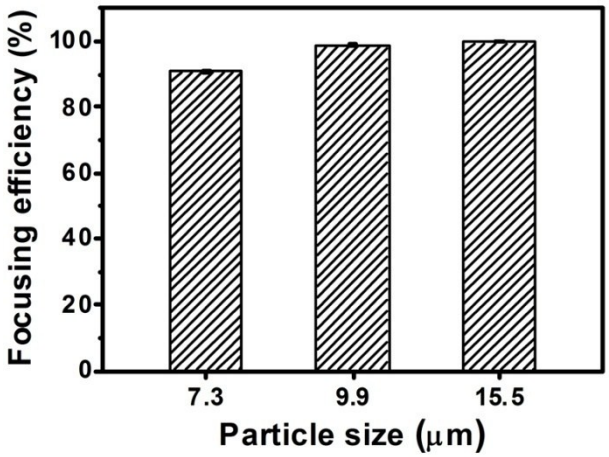

Fig. S13. Focusing efficiency of different-sized particles (7.3, 9.9, and 15.5 μm in diameter) at a high flow rate of 3 ml min^{-1} (Re = 200). Standard deviations deduced from ten parallel experiments are shown as the error bars.

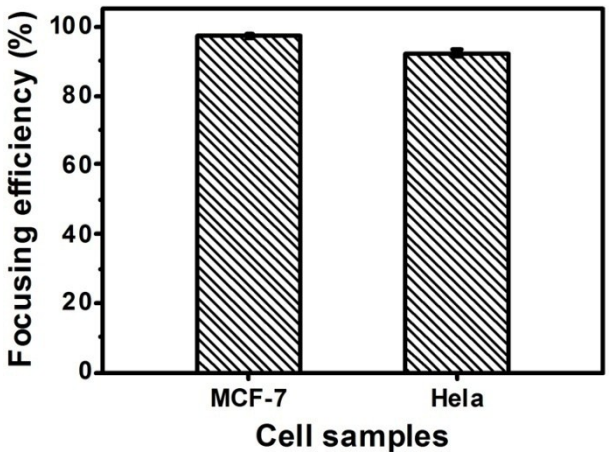

Fig. S14. Focusing efficiency of different cells (MCF-7 and Hela) at a high flow rate of 3 ml min^{-1} (Re = 200). Standard deviations deduced from ten parallel experiments are shown as the error bars

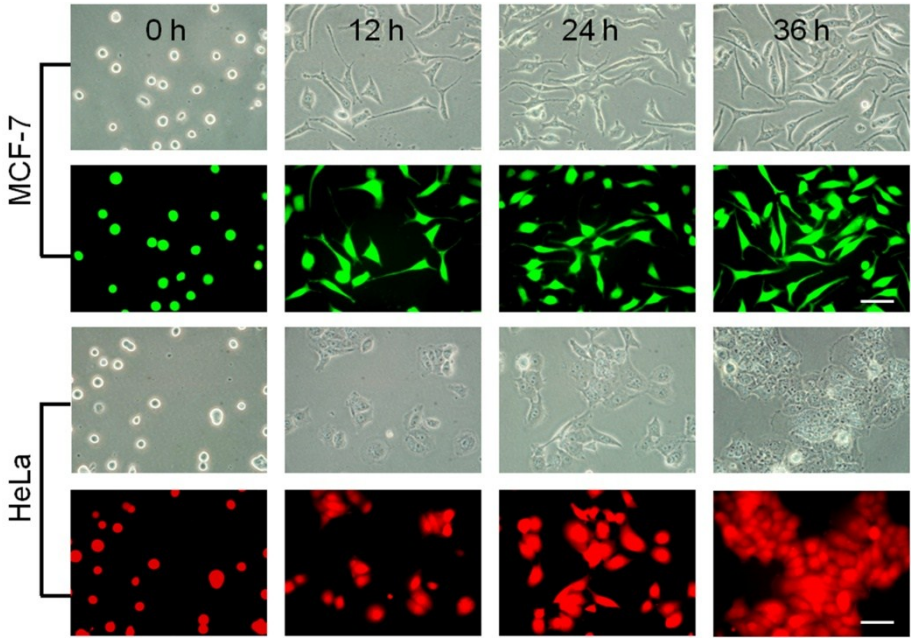

Fig. S15. Cell growth of MCF-7 and HeLa cells by reseeding them back into culture for 36 h after collection from the cell focusing process. Scale bar, 50 μm.

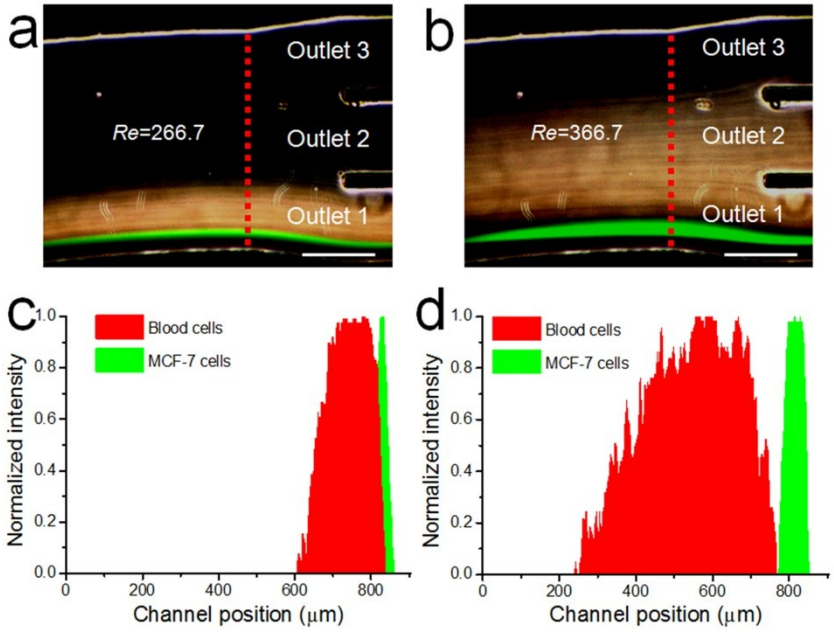

Fig. S16. Rare tumor cell separation using optimized device 3. (a, b) MCF-7 cell focusing (green) at flow rate of 4 and 5.5 ml min^{-1} (Re = 266.7 and 366.7, respectively). The MCF-7 cell-to-blood cell ratio of sample is $1/10^5$. The red dotted lines are used to analyze cell distributions at the same longitudinal positions. (c, d) Analysis of MCF-7 cell separation from blood. The analytical results listed in c and d, correspond to a and b, respectively. Scale bars, 300 μm.

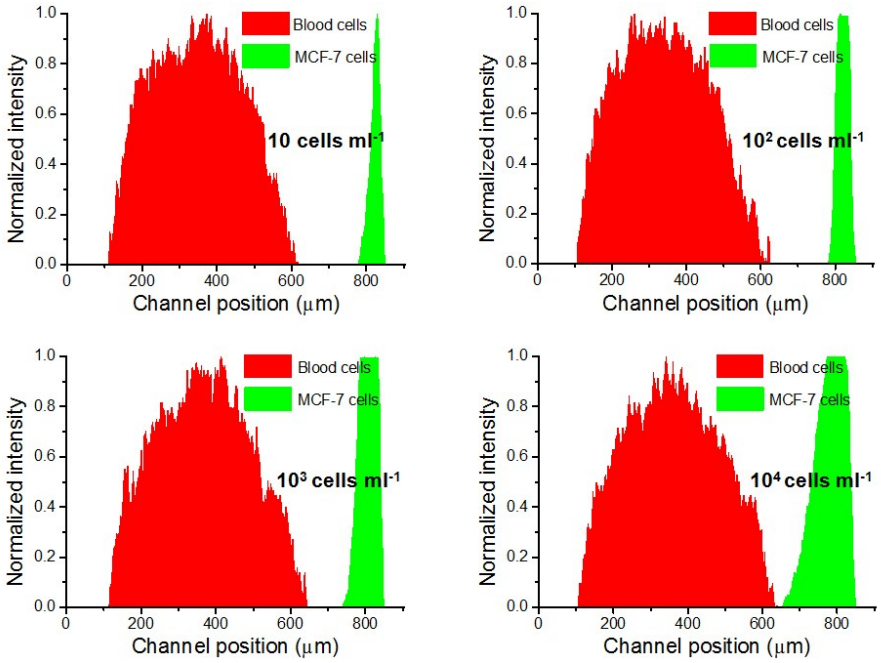

Fig. S17. Assessment of MCF-7 cell separation from blood at different concentrations of tumor cells (10^1–10^4 cells ml^{-1} in 2.5% Hct blood) under Re = 433.3 in the design-optimized device 3. The quantitative results are corresponding to the red dotted lines in Fig.5a.

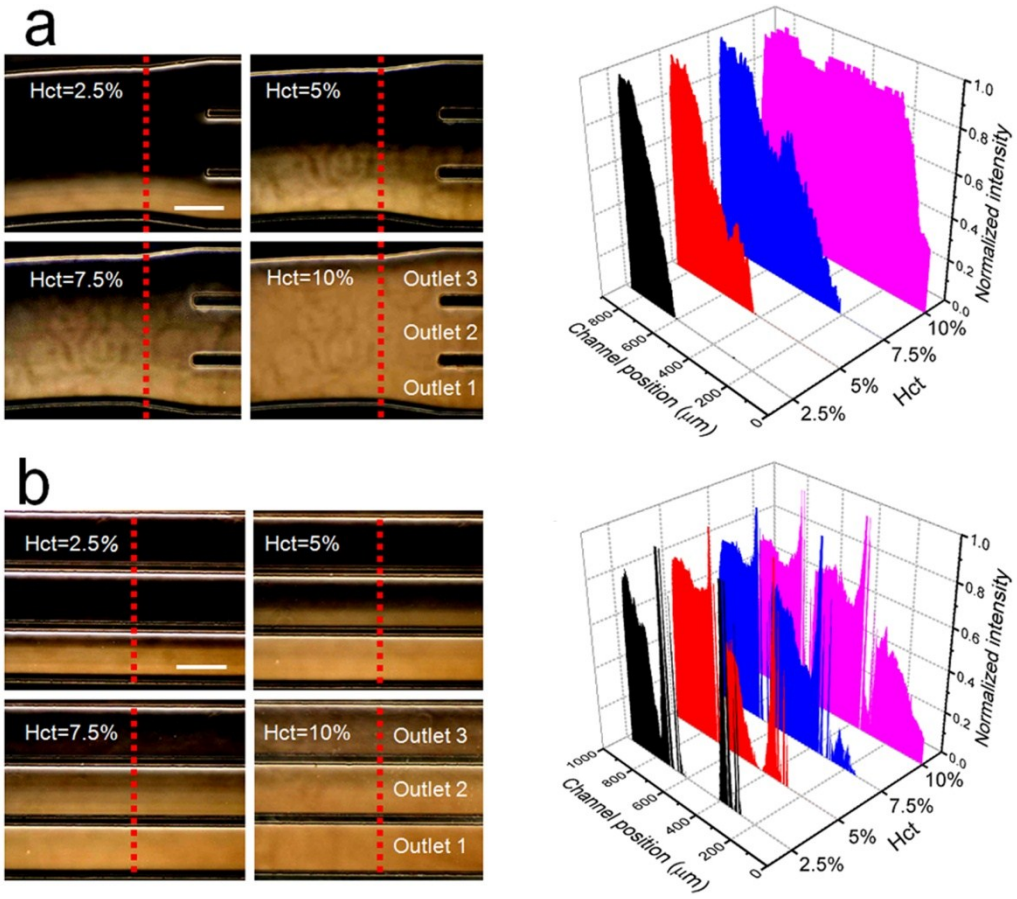

Fig. S18. Plasma extraction from blood with different Hct (2.5% to 10%). (a, b) Effects of Hct on blood cell trajectories in the trifurcated region D (a, left) and outlet region (b, left) of the design-optimized device 3 under Re = 200. The red dotted lines are used to analyze blood cell distributions (right) at the same longitudinal positions. Scale bar, 300 μm.

ESI Movies

Movie S1. Dynamic trajectories of 15.5-μm fluorescent particles in the region C of device 3 with rapidly changing *Re*. Time-lapse fluorescence images were acquired continuously when Re rapidly increased from 0.7 (0.01 ml min^{-1}) to 500 (7.5 ml min^{-1}) within 4 s and then decreased to the initial Re. The Re increasing from 0.7 to 500 was adjusted by directly setting the flow rate from 0.01 ml min^{-1} to 7.5 ml min^{-1} using syringe pump.

Movie S2. Dynamic trajectories of 15.5-μm fluorescent particles in the region E of device 3 with rapidly changing *Re*. Time-lapse fluorescence images were acquired continuously when Re rapidly increased from 0.7 (0.01 ml min^{-1}) to 500 (7.5 ml min^{-1}) within 4 s and then decreased to the initial Re. The Re increasing from 0.7 to 500 was adjusted by directly setting the flow rate from 0.01 ml min^{-1} to 7.5 ml min^{-1} using syringe pump.

Movie S3. Stable trajectories of 15.5-μm fluorescent particles in the region C of device 3. Time-lapse fluorescence images were acquired continuously when particles formed a single-stream focusing under a wide range of Re (100 to 333.3, flow rate: 1.5 ml min^{-1} to 5 ml min^{-1}).

Movie S4. Stable trajectories of 15.5-μm fluorescent particles in the region E of device 3. Time-lapse fluorescence images were acquired continuously when particles formed a single-stream focusing under a wide range of Re (100 to 333.3, flow rate: 1.5 ml min^{-1} to 5 ml min^{-1}).

Movie S5. Stable trajectories of mixed particles (7.3, 9.9, and 15.5 μm in diameter) in the region E of device 3. Time-lapse fluorescence images were acquired continuously at different Re (200, 333.3, and 433.3 corresponding to the flow rates of 3, 5, and 6.5 ml min^{-1} respectively).

Movie S6. Single-stream focusing of MCF-7 cells in the region E of design-optimized device 3 at a flow rate of 3 ml min^{-1} (Re = 200).

Movie S7. Stable trajectories of MCF-7 cells (spiked in diluted whole blood) in the region D of optimized device 3. Time-lapse superimposed images were acquired continuously, showing the separation of MCF-7 cells (10^3 cells ml^{-1}, spiked in 2.5% Hct blood) at a high Re = 433.3 (6.5 ml

min^{-1}). The MCF-7 cells (green) passed through the outlet 1, whereas most blood cells exited through the outlet 2 and outlet 3.

Movie S8. Stable trajectories of blood cells in the region D of optimized device 3. Time-lapse optical images were acquired continuously when blood cells (2.5% Hct) formed a single-band at a flow rate of 3 ml min^{-1} (Re = 200).